

## Research Article

## Fullerene nanosheets for surface-enhanced Raman spectroscopy

 Linchangqing Yang<sup>a,b</sup>, Yahui Li<sup>b</sup>, Wei Liu<sup>b</sup>, Junhao Zhang<sup>c</sup>, Qinghong Kong<sup>a,\*</sup>,  
 Guangcheng Xi<sup>b,\*</sup>
<sup>a</sup> School of the Environment and Safety Engineering, Jiangsu University, Zhenjiang 212013, China<sup>b</sup> Key Laboratory of Consumer Product Quality Safety Inspection and Risk Assessment for State Market Regulation, Chinese Academy of Inspection and Quarantine, Beijing 100176, China<sup>c</sup> School of Environmental and Chemical Engineering, Jiangsu University of Science and Technology, Zhenjiang 212013, China

## ARTICLE INFO

## Keywords:

 Fullerenes  
 Nanosheets  
 Raman sensing  
 Interfacial charge transfer  
 Pollutant detection

## ABSTRACT

Most surface-enhanced Raman scattering (SERS) substrates are based on noble metals or transition metal semiconductors. Developing nonmetallic SERS substrates is of great significance for expanding the application scope of SERS substrate materials. In this study, ultrathin C<sub>60</sub> nanosheets with two-dimensional structures were synthesized using CVD and used as SERS substrates. Owing to the combined effects of favorable factors such as the expanded specific surface area and matched interfacial charge transport paths, the substrate has a minimum detection limit of 10<sup>-11</sup> for rhodamine 6G and a Raman enhancement factor of 10<sup>7</sup>. In addition, the C<sub>60</sub> nanosheets exhibited good stability and uniformity as SERS substrates.

Surface-enhanced Raman spectroscopy (SERS) is a commonly used analytical technique in chemistry [1–3], biology [4–6], and medical science because of its nondestructive nature [7–9], rapid analysis capabilities, and high sensitivity. To achieve optimal performance in terms of sensitivity, stability, and uniformity, researchers have actively explored and developed diverse substrate materials for SERS applications [10,11]. Noble metals such as Au and Ag are the most frequently studied substrates [12–15]. In addition, owing to the advancement of surface plasmon resonance (SPR) technology, various types of semiconductors with SPR effects have been applied to SERS substrates, exhibiting excellent SERS performance [16–19]. However, there are few reports on nonmetallic SERS substrates with superior performance [20]. The development of nonmetallic substrates is of great significance for exploring the mechanism of SERS signal enhancement and expanding the application scope of SERS substrate materials.

Since the discovery of fullerenes in the 1980s [21], their unique structures and properties have attracted widespread attention. The existence of the C<sub>60</sub> conjugated  $\pi$  system endows it with unique electronic properties, including good electron affinity [22], high electron mobility [23], and excellent optoelectronic properties [24,25]. Therefore, C<sub>60</sub> materials are widely used in transistors [26,27], solar cells [28,29], photodetectors [30], and other applications. According to different application scenarios, various methods such as the template method [31,32], chemical vapor deposition (CVD) [33,34], and liquid-liquid interface precipitation (LLIP) [35,36] have been used to synthesize various C<sub>60</sub> micro/nanostructures. CVD is considered a promising method for the

preparation of two-dimensional (2D) materials, including various types of metal and nonmetallic films [37,38]. Carbon materials, which are non-metallic materials, have attracted significant attention. Furthermore, existing research has shown that 2D carbon materials exhibit significant diversity in their physical properties, particularly tunable bandgaps [39,40], which have a significant impact on the performance of nonmetallic SERS substrates.

In this study, we prepared C<sub>60</sub> nanosheets with 2D structure by CVD. These C<sub>60</sub> nanosheets have ultrathin thickness, good crystallinity, and an expanded specific surface area. Using ultrathin C<sub>60</sub> nanosheets as the SERS substrate and rhodamine 6G (R6G) as the detected molecule, multiple matching interfacial charge transport (ICT) paths were observed in the R6G-C<sub>60</sub> nanosheet system. In addition, ultrathin C<sub>60</sub> nanosheets as SERS substrates exhibit excellent stability and uniformity, with an enhancement factor (EF) and detection limits of 10<sup>7</sup> and 10<sup>-10</sup> M, respectively.

To synthesize C<sub>60</sub> samples with 2D structures, we first investigated the experimental conditions. The TGA results of the purchased C<sub>60</sub> powder showed a significant drop in the thermogravimetric curve around 644 °C, corresponding to the sublimation of C<sub>60</sub> (Fig. S1). Therefore, the CVD synthesis method requires a temperature controlled slightly below 644 °C. A temperature that is too low temperature is not conducive to the sublimation of C<sub>60</sub>, while too high can easily lead to the graphitization of C<sub>60</sub>. Notably, the Mg powder plays a key role in the formation of nanosheets. For comparison, magnesium powder was replaced with copper nanopowder and sodium chloride under the same experimental

\* Corresponding authors.

E-mail addresses: kongqh@ujs.edu.cn (Q. Kong), xiguangcheng@caiq.org.cn (G. Xi).

<https://doi.org/10.1016/j.chphma.2024.04.001>

Received 18 March 2024; Received in revised form 20 April 2024; Accepted 30 April 2024

Available online 9 May 2024

2772-5715/© 2024 The Authors. Publishing Services by Elsevier B.V. on behalf of KeAi Communications Co. Ltd. This is an open access article under the CC BY-NC-ND license (<http://creativecommons.org/licenses/by-nc-nd/4.0/>)

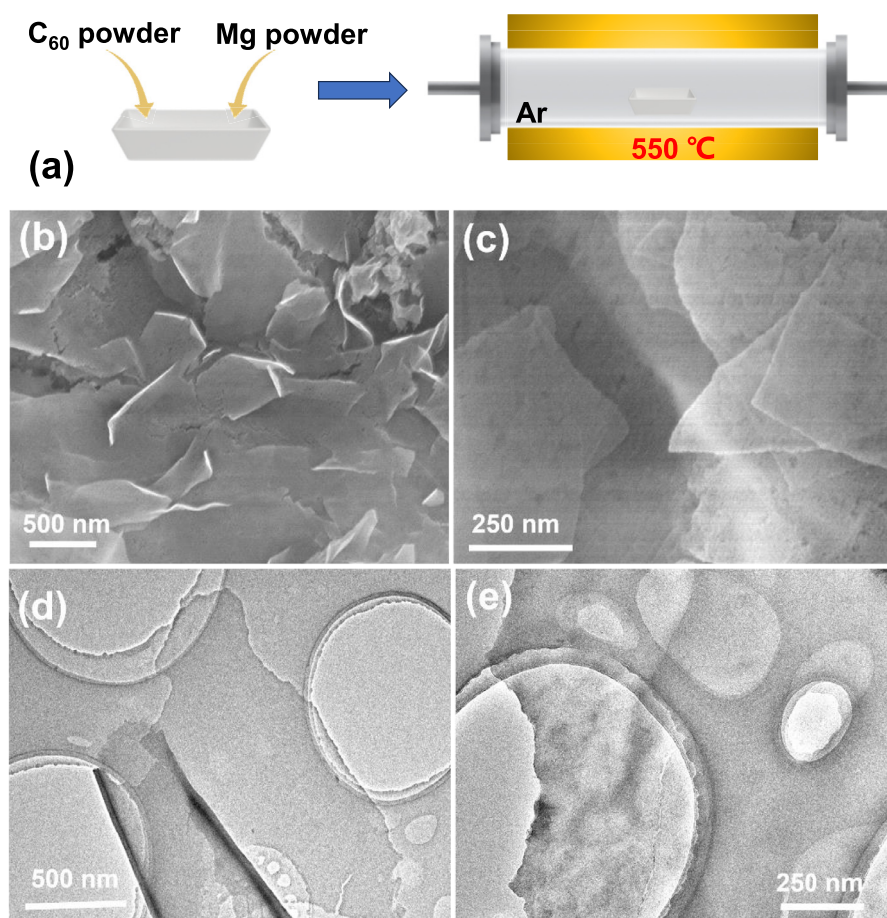


**Fig. 1.** Morphology and structure characterization of the  $C_{60}$  nanosheets. (a) Schematic illustrating the synthesis of the  $C_{60}$  nanosheets. (b)(c) SEM images of  $C_{60}$  nanosheets. (d)(e) TEM images of  $C_{60}$  nanosheets.

conditions; however, no nanosheets were produced (Fig. S2). This may be due to the formation of Mg–C bonds between the magnesium and  $C_{60}$  molecules, which are between covalent and electrovalent bonds. Compared with copper or sodium chloride, which are linked only by weak van der Waals forces, this bond is more conducive to  $C_{60}$  attachment growth [39,41].

Fig. 1(a) shows a schematic of the synthesis of the ultrathin  $C_{60}$  nanosheets using CVD. The original  $C_{60}$  powder was thoroughly ground and placed upstream of the porcelain boat, followed by the magnesium powder, which was placed downstream. The porcelain boat was placed in the tube furnace filled with Ar gas and heated to 550 °C for 10 h, then naturally cooled to room temperature. Scanning electron microscopy (SEM) images (Figs. 1(b)(c)) show that many nanosheets were generated on the Mg powder particles. The surfaces of these nanosheets are smooth and exhibit good uniformity with on-surface cracks, indicating that the growth process is continuous. The size of the nanosheets ranges from a few micrometers to more than ten micrometers (Fig. S3), while these nanosheets were not found on the original  $C_{60}$  particles (Fig. S4). It is important to note that a low gas flow rate is required during the heating process because an excessively high flow rate is detrimental to nanosheet deposition. The morphology and microstructure of the products were analyzed by transmission electron microscopy (TEM). These nanosheets have clear edges and no pores on their surfaces (Figs. 1(d)(e)). In addition, the nanosheets are nearly transparent, indicating that they are extremely thin. The HRTEM images show that these nanosheets have clear lattice structures, indicating that they are highly crystalline (Fig. S5). Energy-dispersive X-ray spectroscopy (EDS) showed that these nanosheets consisted of carbon and a small amount of oxygen, which

was attributed to the oxygen adsorbed on the surface of the nanosheets (Fig. S6).

The chemical compositions and states of the products were analyzed by X-ray diffraction (XRD). In the XRD pattern of the powder product (Fig. S7), three smaller peaks at 10.8°, 17.7°, and 20.7° are observed, corresponding to the (111), (220), and (311) crystal planes of face-centered cubic lattice  $C_{60}$ , respectively. The other three stronger peaks correspond to the (110), (002), and (101) crystal planes of Mg metal, indicating that the powder contained a large amount of Mg powder in addition to  $C_{60}$ . After removing the metallic Mg with dilute hydrochloric acid, pure  $C_{60}$  was obtained, and the characteristic peak of the metallic Mg in the XRD pattern disappeared (Fig. 2(a)). There was almost no difference between the Raman and UV–vis spectra, indicating that the chemical structure of the product remained unchanged after acid treatment (Figs. S8 and S9). Raman spectroscopy is an important means of characterizing  $C_{60}$ , and the Raman spectra of the nanosheets exhibit distinct  $C_{60}$  peaks (Fig. 2(b)). The characteristic peaks at 503 and 1473  $\text{cm}^{-1}$  correspond to typical  $A_g$  vibrational modes, whereas the Raman peaks at 439, 714, 779, 1428, and 1577  $\text{cm}^{-1}$  correspond to active  $H_g$  vibrational modes [40]. X-ray photoelectron spectroscopy (XPS) was used to analyze the atomic composition and valence state of  $C_{60}$  nanosheets. The results show that the  $C_{60}$  nanosheets mainly contain energy level peaks of C and O, and no energy level peaks of Mg (Fig. 2(c)). The presence of oxygen was due to the oxidation and functionalization of the sample surface. The XPS C 1s core level peaks of  $C_{60}$  nanosheets can be deconvoluted into four peaks at 284.2, 285.3, 286.7, and 289.0 eV corresponding to C=C ( $sp^2$ ), C–C ( $sp^3$ ), C–O, and C=O, respectively (Fig. 2(d)).

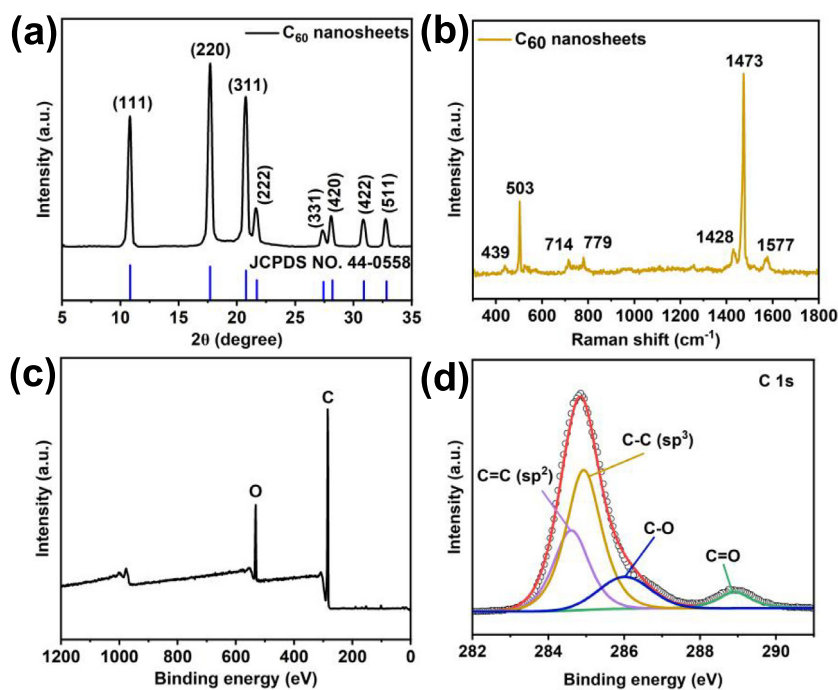


Fig. 2. Component analysis of the  $C_{60}$  nanosheets. (a) XRD pattern of the  $C_{60}$  nanosheets. (b) Raman spectra of the  $C_{60}$  nanosheets. (c) XPS survey spectrum of the  $C_{60}$  nanosheets. (d) C 1s deconvoluted XPS spectra of  $C_{60}$  nanosheets.

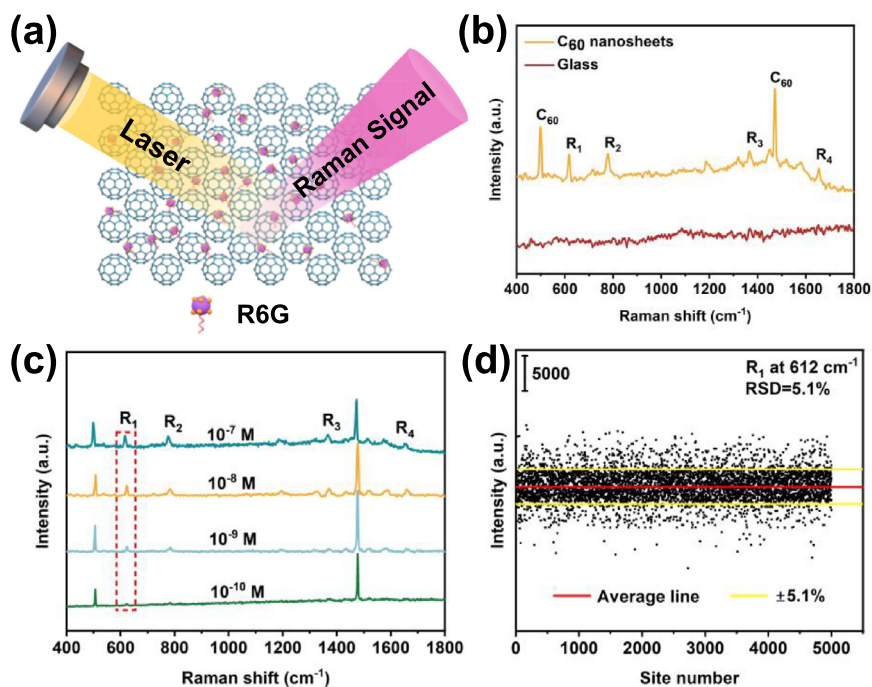
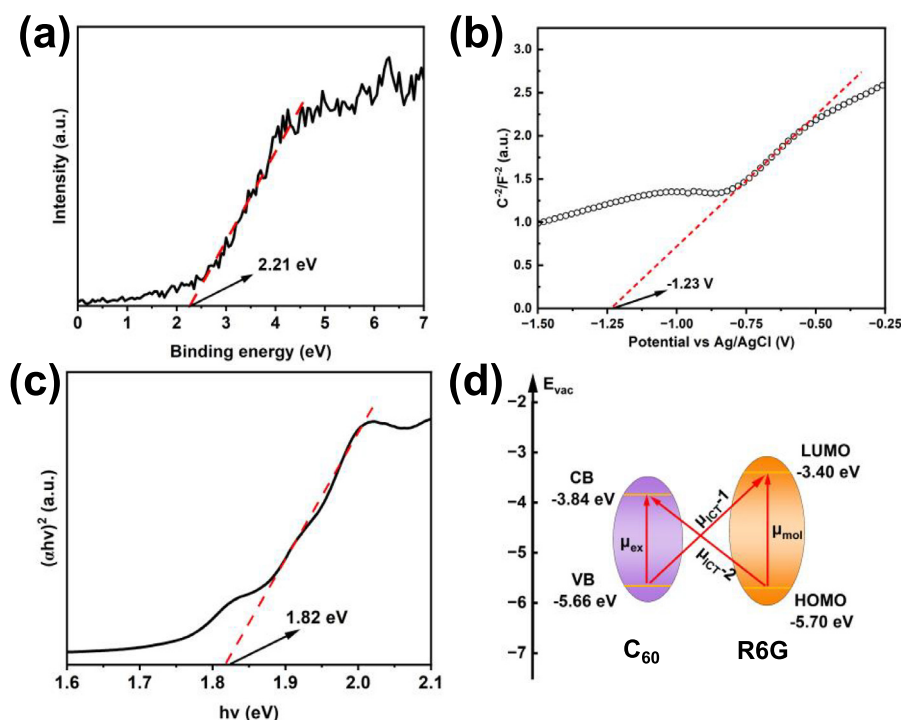


Fig. 3. SERS properties of the  $C_{60}$  nanosheets. (a) Diagram of SERS test. (b) SERS spectra of R6G samples recorded on  $C_{60}$  nanosheets and glass. (c) SERS spectra of  $1 \times 10^{-7}$  to  $1 \times 10^{-10}$  M R6G on  $C_{60}$  nanosheets. (d) RSD of SERS signal intensities at 5000 sites.

We investigated the SERS properties of the ultrathin  $C_{60}$  nanosheets (Fig. 3(a)). Ultrathin  $C_{60}$  nanosheets as the SERS substrate,  $10^{-6}$  M solution of R6G was used for detection. Four characteristic peaks were detected under 532 nm laser excitation (Fig. 3(b)):  $R_1$  ( $612 \text{ cm}^{-1}$ ),  $R_2$  ( $773 \text{ cm}^{-1}$ ),  $R_3$  ( $1363 \text{ cm}^{-1}$ ), and  $R_4$  ( $1652 \text{ cm}^{-1}$ ). Using glass slides under the same conditions, no characteristic peak of R6G was obtained. The results of the comparison experiment exclude the influence of glass slides on the SERS effect, indicating that the enhanced Raman signal originates from the ultrathin  $C_{60}$  nanosheets. Using different concentra-

tions of the R6G solution for detection (Fig. 3(c)), the results showed that the ultrathin  $C_{60}$  nanosheets had a significant Raman enhancement effect in the concentration range of  $10^{-7}$ – $10^{-10}$  M, with a minimum detection limit of  $10^{-11}$  M (Fig. S10). At a concentration of  $10^{-10}$  M, the enhancement factor of ultrathin  $C_{60}$  nanosheets for R6G molecules was approximately  $5.53 \times 10^7$  (detailed calculations are provided in the Supporting Information). In addition to their excellent sensitivity, ultrathin  $C_{60}$  nanosheets as SERS substrates exhibited good signal distribution. The relative standard deviation of the sample substrate was 5.1% when



**Fig. 4.** SERS enhancement mechanism of the  $C_{60}$  nanosheets. (a) XPS valence spectrum of  $C_{60}$  nanosheets. (b) Mott–Schottky plots of the  $C_{60}$  nanosheets. (c) The Tauc plot curve of  $C_{60}$  nanosheets. (d) Band energy alignment diagram of the charge-transfer pathways in  $C_{60}$  and R6G.

the detected intensities of 5000 random Raman signals ( $612\text{ cm}^{-1}$ ) were counted (Fig. 3(d)).

The excellent SERS properties of the ultrathin  $C_{60}$  nanosheets resulted from a combination of many aspects. The ultrathin 2D planar structure provides  $C_{60}$  nanosheets with a larger specific surface area (Fig. S11), which is beneficial for contacting more molecules to be detected and promoting SERS sensing. In addition, the matched interfacial charge transport (ICT) pathways in the R6G- $C_{60}$  ultrathin nanosheet system contributed significantly to the SERS effect [18,42]. The valence band of the sample was obtained from the XPS valence band spectrum (Fig. 4(a)) and the Mott–Schottky curve (Fig. 4(b)), and the conduction band was obtained from the band gap (Fig. 4(c)). Therefore, the valence band energy level of the  $C_{60}$  nanosheets is  $-5.66\text{ eV}$ , and the conduction band energy level is  $-3.84\text{ eV}$ . The HOMO energy level of R6G is known to be  $-5.70\text{ eV}$ , and the LUMO energy level is  $-3.40\text{ eV}$ . Under excitation with the  $532\text{ nm}$  laser ( $2.33\text{ eV}$ ) (Fig. 4(d)), in addition to exception resonance ( $\mu_{\text{ex}}$ ) and molecular resonance ( $\mu_{\text{mol}}$ ), there are at least two matching energy levels in the R6G- $C_{60}$  nanosheet system for the photocatalytic ICT pathway ( $\mu_{\text{ICT-1}}$ :  $2.26\text{ eV}$  and  $\mu_{\text{ICT-2}}$ :  $1.86\text{ eV}$ ). These multifaceted factors combined to form ultrathin  $C_{60}$  nanosheets with excellent SERS properties (Table S1).

In summary, we have synthesized ultrathin  $C_{60}$  nanosheets using a simple CVD process and characterized them in detail. These ultrathin  $C_{60}$  nanosheets exhibited excellent SERS effects as 2D carbon materials and can be used as highly sensitive and reproducible nonmetallic SERS substrates. This work not only expands the application of  $C_{60}$  materials in the field of detection but also suggests that the ultrathin  $C_{60}$  nanosheet structure has broad application prospects in solar energy devices, optoelectronic devices, energy storage, and other fields.

#### Declaration of Competing Interest

The authors declare that they have no known competing financial interests or personal relationships that could have appeared to influence the work reported in this paper.

#### CRediT authorship contribution statement

**Linchangqing Yang:** Writing – review & editing, Writing – original draft, Methodology, Investigation. **Yahui Li:** Investigation. **Wei Liu:** Investigation. **Junhao Zhang:** Methodology. **Qinghong Kong:** Writing – original draft, Methodology, Investigation. **Guangcheng Xi:** Conceptualization, Formal analysis.

#### Acknowledgements

This study was financially supported by the Science Foundation of the Chinese Academy of Inspection and Quarantine (2022JK14) and the National Natural Science Foundation of China (22374139).

#### Supplementary materials

Supplementary material associated with this article can be found, in the online version, at [doi:10.1016/j.chphma.2024.04.001](https://doi.org/10.1016/j.chphma.2024.04.001).

#### References

- [1] S.Y. Ding, J. Yi, J.F. Li, B. Ren, D.Y. Wu, R. Panneerselvam, Z.Q. Tian, Nanostructure-based plasmon-enhanced raman spectroscopy for surface analysis of materials, *Nat. Rev. Mater.* 1 (2016) 16021.
- [2] R. Chikkaraddy, B. De Nijs, F. Benz, S.J. Barrow, O.A. Scherman, E. Rosta, A. Demetriadou, P. Fox, O. Hess, J.J. Baumberg, Single-molecule strong coupling at room temperature in plasmonic nanocavities, *Nature* 535 (2016) 127–130.
- [3] S. Schlücker, Surface-enhanced raman spectroscopy: Concepts and chemical applications, *Angew. Chem. Int. Ed.* 53 (2014) 4756–4795.
- [4] Y. Wang, B. Yan, L. Chen, SERS tags: Novel optical nanoprobes for bioanalysis, *Chem. Rev.* 113 (2013) 1391–1428.
- [5] D. Ciialla-May, X.-S. Zheng, K. Weber, J. Popp, Recent progress in surface-enhanced Raman spectroscopy for biological and biomedical applications: From cells to clinics, *Chem. Soc. Rev.* 46 (2017) 3945–3961.
- [6] Y. Hu, H. Cheng, X. Zhao, J. Wu, F. Muhammad, S. Lin, J. He, L. Zhou, C. Zhang, Y. Deng, P. Wang, Z. Zhou, S. Nie, H. Wei, Surface-enhanced Raman scattering active gold nanoparticles with enzyme-mimicking activities for measuring glucose and lactate in living tissues, *ACS Nano* 11 (2017) 5558–5566.
- [7] X. Fu, Z. Cheng, J. Yu, P. Choo, L. Chen, J. Choo, A SERS-based lateral flow assay biosensor for highly sensitive detection of HIV-1 DNA, *Biosens. Bioelectron.* 78 (2016) 530–537.

- [8] L.J. Xu, Z.C. Lei, J. Li, C. Zong, C.J. Yang, B. Ren, Label-free surface-enhanced Raman spectroscopy detection of DNA with single-base sensitivity, *J. Am. Chem. Soc.* 137 (2015) 5149–5154.
- [9] X. Qiao, B. Su, C. Liu, Q. Song, D. Luo, G. Mo, T. Wang, Selective surface enhanced Raman scattering for quantitative detection of lung cancer biomarkers in superparticle@MOF structure, *Adv. Mater.* 30 (2018) 1702275.
- [10] M.J. Banholzer, J.E. Millstone, L. Qin, C.A. Mirkin, Rationally designed nanostructures for surface-enhanced Raman spectroscopy, *Chem. Soc. Rev.* 37 (2008) 885.
- [11] H. Ko, S. Singamaneni, V.V. Tsukruk, Nanostructured surfaces and assemblies as SERS media, *Small* 4 (2008) 1576–1599.
- [12] D.K. Lim, K.S. Jeon, H.M. Kim, J.M. Nam, Y.D. Suh, Nanogap-engineerable Raman-active nanodumbbells for single-molecule detection, *Nature Mater* 9 (2010) 60–67.
- [13] C.E. Talley, J.B. Jackson, C. Oubre, N.K. Grady, C.W. Hollars, S.M. Lane, T.R. Huser, P. Nordlander, N.J. Halas, Surface-enhanced Raman scattering from individual Au nanoparticles and nanoparticle dimer substrates, *Nano Lett.* 5 (2005) 1569–1574.
- [14] Y. Lu, G.L. Liu, L.P. Lee, High-density silver nanoparticle film with temperature-controllable interparticle spacing for a tunable surface enhanced Raman scattering substrate, *Nano Lett.* 5 (2005) 5–9.
- [15] K.L. Wustholz, A.-I. Henry, J.M. McMahon, R.G. Freeman, N. Valley, M.E. Piotti, M.J. Natan, G.C. Schatz, R.P. Van Duyne, Structure–activity relationships in gold nanoparticle dimers and trimers for surface-enhanced Raman spectroscopy, *J. Am. Chem. Soc.* 132 (2010) 10903–10910.
- [16] Q. Zhang, X. Li, Q. Ma, Q. Zhang, H. Bai, W. Yi, J. Liu, J. Han, G. Xi, A metallic molybdenum dioxide with high stability for surface enhanced Raman spectroscopy, *Nat. Commun.* 8 (2017) 14903.
- [17] S. Cong, Y. Yuan, Z. Chen, J. Hou, M. Yang, Y. Su, Y. Zhang, L. Li, Q. Li, F. Geng, Z. Zhao, Noble metal-comparable SERS enhancement from semiconducting metal oxides by making oxygen vacancies, *Nat. Commun.* 6 (2015) 7800.
- [18] X. Wang, W. Shi, S. Wang, H. Zhao, J. Lin, Z. Yang, M. Chen, L. Guo, Two-dimensional amorphous TiO<sub>2</sub> nanosheets enabling high-efficiency photoinduced charge transfer for excellent SERS activity, *J. Am. Chem. Soc.* 141 (2019) 5856–5862.
- [19] Z. Zheng, S. Cong, W. Gong, J. Xuan, G. Li, W. Lu, F. Geng, Z. Zhao, Semiconductor SERS enhancement enabled by oxygen incorporation, *Nat. Commun.* 8 (2017) 1993.
- [20] X. Ling, L. Xie, Y. Fang, H. Xu, H. Zhang, J. Kong, M.S. Dresselhaus, J. Zhang, Z. Liu, Can graphene be used as a substrate for Raman enhancement? *Nano Lett.* 10 (2010) 553–561.
- [21] H.W. Kroto, J.R. Heath, S.C. O'Brien, R.F. Curl, R.E. Smalley, C<sub>60</sub>: Buckminsterfullerene, *Nature* 318 (1985) 162–163.
- [22] X.B. Wang, C.F. Ding, L.S. Wang, High resolution photoelectron spectroscopy of C<sub>60</sub><sup>-</sup>, *J. Chem. Phys.* 110 (1999) 8217–8220.
- [23] D. Im, H. Moon, M. Shin, J. Kim, S. Yoo, Towards gigahertz operation: Ultrafast low turn-on organic diodes and rectifiers based on C<sub>60</sub> and tungsten oxide, *Adv. Mater.* 23 (2011) 644–648.
- [24] J. Jeng, Y. Chiang, M. Lee, S. Peng, T. Guo, P. Chen, T. Wen, CH<sub>3</sub>NH<sub>3</sub>PbI<sub>3</sub> perovskite/fullerene planar-heterojunction hybrid solar cells, *Adv. Mater.* 25 (2013) 3727–3732.
- [25] R. Pandey, A.A. Gunawan, K.A. Mkhoyan, R.J. Holmes, Efficient organic photovoltaic cells based on nanocrystalline mixtures of boron subphthalocyanine chloride and C<sub>60</sub>, *Adv. Funct. Mater.* 22 (2012) 617–624.
- [26] H. Li, B.C.K. Tee, J.J. Cha, Y. Cui, J.W. Chung, S.Y. Lee, Z. Bao, High-mobility field-effect transistors from large-area solution-grown aligned C<sub>60</sub> single crystals, *J. Am. Chem. Soc.* 134 (2012) 2760–2765.
- [27] K. Itaka, M. Yamashiro, J. Yamaguchi, M. Haemori, S. Yaginuma, Y. Matsumoto, M. Kondo, H. Koinuma, High-mobility C<sub>60</sub> field-effect transistors fabricated on molecular-wetting controlled substrates, *Adv. Mater.* 18 (2006) 1713–1716.
- [28] K. Schulze, C. Uhrich, R. Schüppel, K. Leo, M. Pfeiffer, E. Brier, E. Reinold, P. Bäuerle, Efficient vacuum-deposited organic solar cells based on a new low-bandgap oligothiophene and fullerene C<sub>60</sub>, *Adv. Mater.* 18 (2006) 2872–2875.
- [29] W. Li, K.H. Hendriks, W.S.C. Roelofs, Y. Kim, M.M. Wienk, R.A.J. Janssen, Efficient small bandgap polymer solar cells with high fill factors for 300 nm thick films, *Adv. Mater.* 25 (2013) 3182–3186.
- [30] J.D. Zimmerman, V.V. Diev, K. Hanson, R.R. Lunt, E.K. Yu, M.E. Thompson, S.R. Forrest, Porphyrin-tape/C<sub>60</sub> organic photodetectors with 6.5% external quantum efficiency in the near infrared, *Adv. Mater.* 22 (2010) 2780–2783.
- [31] M.R. Benziger, S. Joseph, H. Ilbeygi, D. Park, S. Sarkar, G. Chandra, S. Umamathy, S. Srinivasan, S.N. Talapaneni, A. Vinu, Highly crystalline mesoporous C<sub>60</sub> with ordered pores: A class of nanomaterials for energy applications, *Angew. Chem. Int. Ed.* 130 (2018) 578–582.
- [32] M. Feng, J. Lee, J. Zhao, Yates, H. Petek, Nanoscale templating of close-packed C<sub>60</sub> nanowires, *J. Am. Chem. Soc.* 129 (2007) 12394–12395.
- [33] X. Yu, J. Zhang, W. Choi, J.Y. Choi, J.M. Kim, L. Gan, Z. Liu, Cap formation engineering: From opened C<sub>60</sub> to single-walled carbon nanotubes, *Nano Lett.* 10 (2010) 3343–3349.
- [34] H.S. Shin, S.M. Yoon, Q. Tang, B. Chon, T. Joo, H.C. Choi, Highly selective synthesis of C<sub>60</sub> disks on graphite substrate by a vapor–solid process, *Angew. Chem. Int. Ed.* 47 (2008) 693–696.
- [35] X. Li, S. Sun, F. Wu, Y. Miao, C<sub>60</sub> nanorods as a promising infrared nonlinear optical material for ultrafast photonics, *Carbon* 178 (2021) 728–733.
- [36] M. Sathish, K. Miyazawa, Size-tunable hexagonal fullerene (C<sub>60</sub>) nanosheets at the liquid–liquid interface, *J. Am. Chem. Soc.* 129 (2007) 13816–13817.
- [37] Y.L. Hong, Z. Liu, L. Wang, T. Zhou, W. Ma, C. Xu, S. Feng, L. Chen, M.L. Chen, D.M. Sun, X.Q. Chen, H.M. Cheng, W. Ren, Chemical vapor deposition of layered two-dimensional MoSi<sub>2</sub>N<sub>4</sub> materials, *Science* 369 (2020) 670–674.
- [38] Z. Cai, B. Liu, X. Zou, H.M. Cheng, Chemical vapor deposition growth and applications of two-dimensional materials and their heterostructures, *Chem. Rev.* 118 (2018) 6091–6133.
- [39] L. Hou, X. Cui, B. Guan, S. Wang, R. Li, Y. Liu, D. Zhu, J. Zheng, Synthesis of a monolayer fullerene network, *Nature* 606 (2022) 507–510.
- [40] R.G. Shrestha, L.K. Shrestha, A.H. Khan, G.S. Kumar, S. Acharya, K. Ariga, Demonstration of ultrarapid interfacial formation of 1D fullerene nanorods with photovoltaic properties, *ACS Appl. Mater. Inter.* 6 (2014) 15597–15603.
- [41] E. Meirzadeh, A.E. Evans, M. Rezaee, M. Milich, C.J. Dionne, T.P. Darlington, S.T. Bao, A.K. Bartholomew, T. Handa, D.J. Rizzo, R.A. Wiscons, M. Reza, A. Zangiabadi, N. Fardian-melamed, A.C. Crowther, P.J. Schuck, D.N. Basov, X.Y. Zhu, A. Giri, P.E. Hopkins, P. Kim, M.L. Steigerwald, J.J. Yang, C. Nuckolls, X. Roy, A few-layer covalent network of fullerenes, *Nature* 613 (2023) 71–76.
- [42] X. Wang, W. Shi, G. She, L. Mu, Using Si and Ge nanostructures as substrates for surface-enhanced Raman scattering based on photoinduced charge transfer mechanism, *J. Am. Chem. Soc.* 133 (2011) 16518–16523.